

FLAME: Fitting Ly α Absorption lines using Machine learning

Priyanka Jalan¹, Vikram Khaire^{2,3}, M. Vivek⁴, and Prakash Gaikwad⁵

¹ Center for Theoretical Physics of the Polish Academy of Sciences, Al. Lotników 32/46, 02-668 Warsaw, Poland
e-mail: priyajalan14@gmail.com

² Indian Institute of Space Science and Technology, Thiruvananthapuram, Kerala 695547, India

³ Physics Department, Broida Hall, University of California Santa Barbara, Santa Barbara, CA 93106-9530, USA

⁴ Indian Institute of Astrophysics, Koramangala, Bengaluru, Karnataka 560034, India

⁵ Max-Planck-Institut für Astronomie, Königstuhl 17, D-69117 Heidelberg, Germany

ABSTRACT

We introduce FLAME, a machine learning algorithm designed to fit Voigt profiles to H I Lyman-alpha (Ly α) absorption lines using deep convolutional neural networks. FLAME integrates two algorithms: the first determines the number of components required to fit Ly α absorption lines, and the second calculates the Doppler parameter b , the H I column density N_{HI} , and the velocity separation of individual components. For the current version of FLAME, we trained it on low-redshift Ly α forests observed with the Far Ultraviolet gratings of the Cosmic Origin Spectrograph (COS) aboard the Hubble Space Telescope (HST). Drawing on this data, we trained FLAME on $\sim 10^6$ simulated Voigt profiles, forward-modeled to mimic Ly α absorption lines observed with HST-COS, to classify lines as either single or double components and then determine Voigt profile fitting parameters. FLAME shows impressive accuracy on the simulated data by identifying more than 98% (90%) of single (double) component lines. It determines b values within $\approx \pm 8$ (15) km s⁻¹ and $\log N_{\text{HI}}/\text{cm}^2$ values within $\approx \pm 0.3$ (0.8) for 90% of the single (double) component lines. However, when applied to real data, FLAME's component classification accuracy drops by $\sim 10\%$. Despite this, there is a reasonable agreement between the b and N_{HI} distributions obtained from traditional Voigt profile fitting methods and FLAME's predictions. Our mock HST-COS data analysis, designed to emulate real data parameters, demonstrated that FLAME could achieve consistent accuracy comparable to its performance with simulated data. This finding suggests that the drop in FLAME's accuracy when used on real data primarily arises from the difficulty of replicating the full complexity of real data in the training sample. Nevertheless, FLAME's performance validates the use of machine learning for Voigt profile fitting, underscoring the significant potential of machine learning for detailed analysis of absorption lines.

Key words. quasars: general – quasars: voigt profile

1. Introduction

The gas that permeates the space between galaxies is called an Intergalactic medium (IGM). One of the premier tools to explore the IGM is studying a swath of Ly α absorption lines present in quasar spectra known as the Ly α forest (Rauch 1998; Meiksin 2009). These absorption lines result from the quasar's continuum being absorbed by the redshifted Ly α (1215.67 Å) resonance line of the neutral hydrogen gas. The Ly α forest has been shown to be an exceptional tool for studying the thermal state of the IGM (e.g. Schaye 2001; Bolton et al. 2008; Lidz et al. 2011; Hiss et al. 2018; Gaikwad et al. 2021; Hu et al. 2023), the intensity of the ionizing ultraviolet background (e.g. Bolton & Haehnelt 2007; Becker et al. 2013; Gaikwad et al. 2017; Khaire et al. 2019; Hu et al. 2023), and a wide range of cosmological parameters, including the mass of neutrinos (McDonald et al. 2006; Baur et al. 2017; Yèche et al. 2017), and dark matter properties (Busca et al. 2013; Viel et al. 2013; Iršič et al. 2017; Alam et al. 2021).

The Ly α forest at high redshift shows remarkable consistency with theoretical expectations from the IGM, such as the expected Gunn-Peterson troughs in $z \sim 6$ quasar spectra (Fan et al. 2006; Bosman et al. 2018; Eilers et al. 2018) and the peak in temperature around the epoch of He II reionization (e.g. Walther et al. 2019; Gaikwad et al. 2021) which is believed to conclude around $z \sim 3$ (McQuinn et al. 2009; Shull et al. 2010; Worseck et al. 2011; Khaire 2017).

In contrast, the low-redshift ($z < 1$) Ly α forest has yielded several unexpected results, prompting new investigations. For instance, the distribution of line widths in the Ly α forest at $z < 0.5$ is broader than what simulations of the IGM can reproduce (Viel et al. 2017; Gaikwad et al. 2017) and there is evidence of a higher-than-expected temperature at $z \sim 1$ (Hu et al. 2023). Furthermore, the epoch $z < 1$ is critically important for galaxy formation, as it is during this period that feedback from galaxy formation (Springel 2005; Hopkins et al. 2008; Bolton et al. 2017; Weinberger et al. 2017; Davé et al. 2019) is believed to have a significant impact on the galaxies in order to explain the observed properties of galaxies and the sharp decline in star formation history (Madau & Dickinson 2014; Khaire & Srianand 2015). Additionally, this is the epoch where more than 30% of baryons are still not accounted for (Shull et al. 2012) in observation (however see de Graaff et al. 2019; Tanimura et al. 2019; Macquart et al. 2020). Moreover, the degree to which galaxy formation feedback impacts the low- z IGM is still unclear (Khaire et al. 2023; Tillman et al. 2022). Whereas simulations, even with extreme feedback, are yet unable to reproduce the line width distribution of the low- z Ly α forest (Gurvich et al. 2017; Bolton et al. 2022; Khaire et al. 2023). Due to these challenges, studying the low- z Ly α forest becomes particularly interesting and crucial for understanding these discrepancies. Therefore, this work focuses mostly on the low- z Ly α forest.

Despite its potential, effectively extracting information from the $\text{Ly}\alpha$ forest has proven to be challenging, especially when it is done via fitting Voigt profiles to the swath of absorption lines. Overlapping lines, varying signal-to-noise ratios, instrumental line spread functions, and other systematics can lead to parameter degeneracies, making it difficult to extract accurate physical information from the data. Usually, for dealing with a swath of $\text{Ly}\alpha$ lines, semi-or fully automated codes for Voigt profile fitting are used, such as “Voigt profile Parameter Estimation Routine” (VIPER Gaikwad et al. 2017, hereafter, G17), BayesVP (Liang & Kravtsov 2017), GVPFIT (Bainbridge & Webb 2017) and VoigtFit (Krogager 2018), however, they are still computationally expensive for large samples.

Moreover, the sheer volume of data from modern surveys demands efficient and automated analysis techniques to handle the increasing workload. It is especially important given the exponential growth in data from ongoing and upcoming surveys such as the Sloan Digital Sky Survey (SDSS Bolton et al. 2012), Dark Energy Spectroscopic Instrument (DESI, Flaugher & Bebek 2014), WEAVE (Pieri et al. 2016), 4MOST (de Jong et al. 2012), providing an unprecedented wealth of absorption spectra for analysis. In this regard, machine learning (ML) techniques offer a promising solution.

ML algorithms, particularly those under the umbrella of deep learning (LeCun et al. 2015; Goodfellow et al. 2016), have demonstrated remarkable competency in pattern recognition, noise handling, and parameter estimation, making them well-suited for the challenges posed by the $\text{Ly}\alpha$ forest. ML models can learn the relationships between input data and desired outputs by training on large datasets of simulated or observed $\text{Ly}\alpha$ forest. Furthermore, ML techniques can improve the efficiency of the fitting process. Automating the analysis using ML models reduces human intervention and subjective bias while enabling rapid analysis of large datasets.

In recent years, various applications of ML techniques have been developed in multiple aspects of cosmology (Akhazhanov et al. 2021; Lee & Shin 2021; Vattis et al. 2021; Liu et al. 2021; de Dios Rojas Olvera et al. 2021). Particularly, deep learning or convolutional neural networks (CNN) are distinguished ways to analyze data. For example, Parks et al. (2018) used CNN to predict HI column density of the damped $\text{Ly}\alpha$. Huang et al. (2021) used a neural network to estimate the $\text{Ly}\alpha$ optical depth values from noisy and saturated transmitted flux data in quasar spectra. Veiga et al. (2021) used a deep neural network to infer the matter density power spectrum from the quasar spectra. Cheng et al. (2022) also used CNN to identify the column density and Doppler widths of the $\text{Ly}\alpha$ lines at high redshifts. Recently, Stemmock et al. (2023) also used deep learning to identify these parameters for Mg II doublet absorption lines.

Motivated by these studies and with the aim of combining the power of ML and the rich information contained within $\text{Ly}\alpha$ forest spectra, we develop FLAME (Fitting $\text{Ly}\alpha$ Absorption lines using Machine Learning); a combination of a two-part algorithm to identify the number of components in each $\text{Ly}\alpha$ absorption system and then fit the Voigt profiles to each. To train these ML models, we generate multiple simulated absorption lines with properties similar to low- z $\text{Ly}\alpha$ absorption lines observed with the Cosmic Origin Spectrograph (COS) on board the Hubble Space Telescope (HST). In addition to the importance mentioned above, we focus our models exclusively on low- z data to avoid complexities since the $\text{Ly}\alpha$ forest is less dense, with minimal blending compared to high-redshift $\text{Ly}\alpha$ forest regions. This allows for easier isolation and fitting of each absorption line system. Nonetheless, even within low- z data, both single and mul-

iple components are present. Therefore, our two-part algorithm FLAME first determines the number of components present and then fits these identified components accordingly.

To assess the robustness of our networks, we evaluate their performance on simulated, real observed (Danforth et al. 2016), and mock datasets. For the real dataset, we compare the model parameters with that derived using vPFIT¹ (Carswell & Webb 2014) and VIPER. Our findings reveal that the neural networks demonstrate comparable performance while requiring significantly lower computational resources.

The paper is organized as follows. We detail the terminologies of the ML algorithms in Sec. 2. Sec. 3 discusses creating and pre-processing the simulated data. We present the model and performances of the two ML algorithms in Sec. 4 and Sec. 5. In Sec. 6, we compare the accuracy of our ML algorithm with the traditional algorithms on the observed data. In Sec. 7, we discuss our key findings on using ML for Voigt profile fitting and summarize in Sec. 8.

2. Machine learning

Machine learning (ML) is a branch of artificial intelligence focused on developing algorithms to learn from data and later can be used to make predictions without explicit programming. ML involves designing statistical and mathematical frameworks to uncover patterns, correlations, and trends within datasets autonomously.

ML can be broadly classified as supervised or unsupervised. The unsupervised ML involves discovering patterns and structures in data without predefined labels. One of the applications is grouping similar data points based on certain features or characteristics. However, the ML model that finds a relation between the features in the measurements (training data) and its defining variables (labels) is known as the supervised ML. This trained model then predicts the label for any given set of measurements; the accuracy of this can be measured using validation data. In this paper, we only discuss supervised ML.

After defining the problem at hand, supervised ML can be summarized in six steps:

- Preparing the training data that includes collecting and pre-processing the data (Sect. 3) with their corresponding labels.
- Splitting the data into training and test/validation datasets. It is important that this splitting is random and that the training and testing cover a similar range of parameters to avoid possible extrapolation problems.
- Generating an ML model and training it on the training dataset and predicting the labels for the testing dataset (Sect. 4.1 and Sect. 5.1).
- Assessing the model’s performance using the test or validation data by comparing the true and predicted labels.
- If the model’s performance is unsatisfactory, adjusting hyperparameters, using different feature sets, or modifying the model architecture,
- Selecting the best-performing model, evaluating its performance (see Sect. 4.2 and Sect. 5.2).

These supervised ML algorithms commonly employ neural networks used across multiple applications.

¹ <http://www.ast.cam.ac.uk/~rfc/vpfit.html>

2.1. Neural Networks and Activation Functions

Neural networks work by sending information through layers of connected nodes or neurons, each contributing to the ability of the network to learn and make predictions. In these networks, every neuron is connected to all neurons in the next layer, and these connections have weights. These weights help determine how important each input is. At each neuron, the inputs are combined into a weighted sum, which is then processed by an activation function. This function is key because it allows the network to handle complex patterns by introducing non-linearities, which are essential for tasks that linear models can not solve. Activation functions let the network handle a wide range of tasks and data patterns, making it capable of doing everything from simple classification to solving intricate problems across different areas. The combination of these linear (weights and inputs) and non-linear (activation functions) elements is what enables neural networks to learn from various data and perform a broad spectrum of tasks, as discussed in Parhi & Nowak (2019).

We use two activation functions in this study, as described below:

(a) Leaky Rectified Linear Unit (*Leaky ReLU*):

$$f(x) = \max(0.01x, x). \quad (1)$$

This function returns x if it receives any positive weighted sum input, but for any negative value of x , it returns a small value of $0.01x$. Therefore, it gives a positive output for negative values as well.

(b) *Sigmoid*:

$$f(x) = \frac{1}{(1 + e^{-x})}. \quad (2)$$

The value of this function exists between 0 to 1. This activation function is beneficial for models that predict the output as a probability, as the probability of anything exists between 0 and 1. We use *sigmoid* at the final layer of the classification model (Sect. 4).

The hierarchical arrangement of layers enables the neural network to learn increasingly “abstract representations” as information progresses through the network. A network containing multiple fully connected layers is known as a Deep neural network. However, to study the structure and patterns present in complex data, Convolutional Neural Networks (CNNs) are designed. In the following subsection, we describe the CNNs.

2.2. Convolutional Neural Network

Convolutional neural networks (CNNs) are specialized neural networks designed for processing data arranged in a grid-like structure, such as images or time series. They are particularly effective at detecting spatial relationships within the input data through a sequence of interconnected layers. In this study, we use CNNs to identify the number of blended Ly α absorption lines and fit Voigt profiles to them.

At the heart of CNNs lie *convolutional layers*, which utilize *filters* to apply convolutions to the input. A *filter* consists of multiple *kernels*, with each *kernel* dedicated to a specific channel of the input. As these *filters* move across the input, they perform element-wise multiplications and summations, generating feature maps in the process. These feature maps are crucial for extracting various data characteristics, such as edges, textures, and patterns. A key hyper-parameter, *stride*, governs the step size of the filter as it scans across the input. *Padding*, another important

parameter, ensures comprehensive coverage of the input’s edges, preserving the size of the input through the convolution process. This study employs the ‘SAME’ padding technique, ensuring that the dimensions of the output post-convolution remain consistent with the input dimensions.

Following the convolutional layers, *Pooling layers* are used to reduce the spatial dimensions of the feature maps, thereby simplifying the information while retaining the most relevant features (Gholamalinezhad & Khosravi 2020). In this study, we use max pooling (Matoba et al. 2022), a technique that identifies and retains the maximum value within a specific region defined by the kernel’s coverage. This approach effectively captures the most prominent features within each region, enhancing the network’s ability to understand spatial hierarchies and relationships.

In the following sub-section, we explore how neural networks are trained and discuss the importance of loss functions in improving their accuracy.

2.3. Neural Network Training and Optimization

After designing the neural network, we optimize the network’s parameters by training the neural network to enable accurate predictions. The training procedure involves two main steps: forward propagation and backpropagation.

During forward propagation, input *training data* flows through the network, with each neuron applying an activation function to the received signals, producing outputs. The computed outcomes are then compared to the true labels using a loss function, such as mean squared error (*MSE*) or cross-entropy, quantifying the error in predictions. For example, in this study, one of the loss functions used is binary cross-entropy (*BCE*), which has a functional form of:

$$H_p(q) = -\frac{1}{N} \sum_{i=1}^N y_i \log(p[y_i]) + (1 - y_i) \log(1 - p[y_i]), \quad (3)$$

$H_p(q)$ signifies the entropy between the predicted probability distribution p and the true distribution q . N represents the dataset’s total number of samples. y_i is the “true label” of the i^{th} sample in the dataset. It can be either 0 or 1 in a binary classification scenario. $p[y_i]$ is the predicted probability that the i^{th} sample belongs to class 1 (or has label 1).

Backpropagation involves propagating the error backward through the network to compute gradients of the loss function with respect to the network’s parameters. These gradients provide valuable information on adjusting the parameters to minimize the error. Popular optimization algorithms, like *Adagrad*, *RMSprop*, Stochastic Gradient Descent (*SGD*), and *Adam* (Kingma & Ba 2014), update the parameters iteratively to minimize these gradients. One of the crucial hyperparameters in ML algorithms is the learning rate. It determines the step size at which the model parameters are updated during the optimization process. This study uses the *Adam* optimizer, which is a more efficient alternative to the other methods, to adjust the model weights.

During training, the network updates its parameters by utilizing smaller subsets or batches of the dataset. This study uses smaller *batch sizes* that allow more frequent updates to the network’s parameters, leading to faster convergence and mitigating memory limitations (You et al. 2017). Another hyperparameter is the number of *epochs* determining how often the network will iterate over the training dataset. We define the epochs for this study by implementing an *early stopping technique*. This

approach halts the training process when the validation performance no longer improves, helps prevent overfitting, and conserves computational resources.

Neural network training relies on a labeled dataset, careful selection of architecture, regularization techniques to prevent overfitting, and hyperparameter tuning to achieve optimal results. We iterate the hyperparameters mentioned above after carefully selecting the data and model. Then, we choose the hyperparameters that produce satisfactory results, measured using an evaluation metric. Below, we discuss the evaluation metrics used in this study.

2.4. Evaluation metrics

After training the network and finding the best hyperparameters, we validate the model using a test or validation dataset. The evaluation metrics of this test dataset ensure the model is unbiased and test its performance. The labels of the testing dataset are called the “true” labels, and the predictions made by the model are known as the “predicted” labels. In this study, we use two models as described in Sect. 4.1 and 5.1; (i) Binary classification algorithm - to classify the number of absorptions into single and double lines, and (ii) Regression algorithm - to identify the Voigt profile parameters of the absorption lines. Therefore, we require two evaluation metrics.

In the binary classification algorithm, there are two classes: positive and negative. To test the performance of the binary classification algorithm (Hossin & M.N 2015), we calculate the accuracy,

$$accuracy = \frac{TP + TN}{TN + FP + FN + TP}, \quad (4)$$

where TP: true positive, TN: true negative, FP: false positive, FN: false negative. The true positives and negatives imply that the model’s outcome correctly predicts the positive and negative classes. The false positive means the model’s outcome incorrectly predicts a positive class for an actual negative class. The false negative means the model’s outcome incorrectly predicts a negative class for an actual positive class.

Other parameters to identify the robustness of the classification algorithm are

- **Sensitivity:** also known as Recall, assesses a model’s ability to correctly identify positive instances, focusing on minimizing false negatives.
- **Specificity:** also known as True Negative Rate, gauges a model’s capacity to recognize negative instances, aiming to minimize false positives accurately.
- **Precision:** quantifies the proportion of correctly predicted positive cases among all instances predicted as positive, emphasizing the minimization of false positives.
- **Negative Predictive Value:** evaluates the proportion of accurately predicted negative cases among all instances predicted as negative, giving insight into the model’s ability to avoid false negatives.

The precision and sensitivity lead to the F1-Score. The F1-score is the harmonic mean of precision and recall as given by,

$$F1\text{-Score} = 2 \times \frac{Precision \times Recall}{Precision + Recall}. \quad (5)$$

It is a single metric that balances both precision and recall and is especially useful when the class distribution is imbalanced. The F1-score ranges between 0 and 1, with higher values

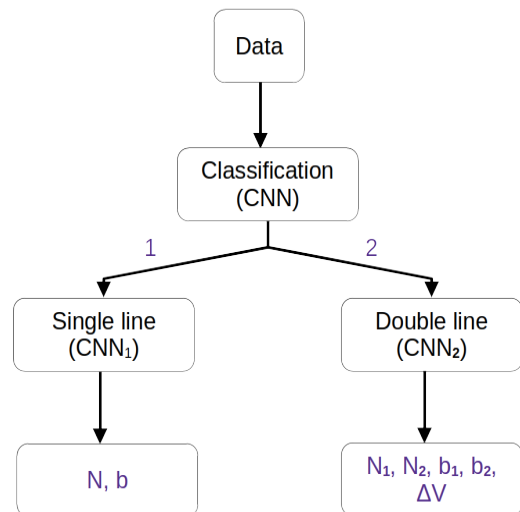


Fig. 1. The flowchart outlines the sequence of three neural networks comprising FLAME. The input training data to the classification algorithm is the normalized flux with 301 array size labeled as 1 or 2 absorption lines. The same input data is then fed to different regression algorithms based on the number of absorption lines. For this algorithm, the labels with the input dataset are the physical parameters like column density and Doppler width.

indicating better performance. An F1 score of 1 indicates perfect precision and recall, while lower scores imply some trade-off between precision and recall. An F1 score around 0.8 indicates a strong balance between precision and recall, suggesting that the model correctly identifies positive cases and avoids false positives.

During the regression analysis (as described in Section. 5), we predict values from the model and compare them to the true labels of the dataset. To test the accuracy of the regression analysis, we use the *MSE*. We also calculate the 90 and 68 percentile values of the absolute differences in the true and predicted values to understand the data distribution and its concentration. We use percentiles because they are less sensitive to extreme values or outliers since they’re based on rank order rather than actual values.

Fig. 1 shows the flowchart sequence of the two models used in this study. The first algorithm is a CNN that classifies the number of absorption lines into either single or double. The choice of only two states is dictated by the low-*z* dataset we used (see Section. 3). Once the classification is performed, we use the second algorithm, which consists of two CNNs, to estimate the features/parameters, one for single lines and the other for double lines. These networks are created using the TensorFlow² interface (Abadi et al. 2015). We construct a simulated dataset of low-*z* Ly α lines and use it to train the networks created here. We outline the details of the dataset in the next section.

3. Training and testing dataset

The training dataset is the initial input to the network during the training process and plays a crucial role in shaping the network’s ability to learn and make predictions. Therefore, we require a

² https://www.tensorflow.org/api_docs/python/tf/keras

well-constructed training dataset that covers a range of parameter space and represents the real-observed data. However, due to the limited sample available of the low- z Ly α absorption lines, we generate our training dataset by simulating Voigt profiles. In order to model realistic simulated Ly α lines, we use the general properties of the observed low- z Ly α data. Below, we explain the properties of the low- z data and how it was used to employed in simulating the lines for training.

3.1. Observational data description

We aim to apply ML techniques to fit low-redshift Ly α lines, drawing on the extensive survey of the low-redshift intergalactic medium (IGM) at $z < 0.48$ conducted by Danforth et al. (2016), henceforth referred to as D16. This survey uses 82 high signal-to-noise ratio (SNR) quasar spectra observed with the HST/COS in the far-ultraviolet (FUV) band using medium-resolution gratings G130M and G160M ($R \sim 18000$, $\Delta v \sim 18 \text{ km s}^{-1}$) across different lifetime positions to cover a wavelength range of 1030 to 1800 Å. D16 combined data from both gratings whenever available, applied manual continuum fitting to each spectrum, and cataloged all absorption lines, including those intervening, associated, and arising from the Milky Way’s interstellar medium.

D16 determined locations of absorption lines using a crude significance level vector $SL(\lambda) = W(\lambda)\bar{\sigma}(\lambda) > 3$, where $W(\lambda)$ represents the equivalent width vector and $\bar{\sigma}(\lambda)$ denotes the error vector in regions without lines. Following this localization, a standard procedure was employed to identify lines by using coincident higher-order lines or lines from different ions. They identified a total of 2611 intervening Ly α lines and modeled them with Voigt profiles. The line list tables from D16, publicly available in the high-level science product at the Mikulski Archive for Space Telescopes³, include details of these fits, such as the Doppler width (b), redshift (z_{abs}), and neutral hydrogen column density (N_{HI}), along with their associated errors.

For the present study, we selected 1917 Ly α lines that are not blended with metal lines or higher-order lines from the D16 catalog. According to D16’s fits, 81.2% (1557) of these lines are single lines, 14.9% (286) are doublet structures, and the remaining 3.8 % (74) consist of three or more lines. We used the parameters of these lines to generate the simulated training dataset described in the following section.

3.2. Simulated data

The simulated Ly α absorption lines are generated with randomly selected (from a uniform distribution) column density ($N_{HI}/[\text{cm}^{-2}]$) and Doppler width ($b/[\text{km s}^{-1}]$) and combined it with instrumental properties of HST/COS data. The range for each parameter includes the minimum and maximum values (for 98.5% data avoiding the outliers in each parameter) of the HST data, as mentioned above. Since the real observed dataset (Sect. 3.1) has $< 4\%$ lines with > 2 components, our simulated dataset is limited to single and double lines. The parameter ranges are as follows:

- Doppler width: $b \text{ (km s}^{-1}\text{)} = 5\text{-}100$,
- Column density: $\log N_{HI} \text{ (cm}^{-2}\text{)} = 12\text{-}17$,
- Signal-to-Noise Ratio: $\text{SNR} = 5\text{-}100$,
- Central wavelength: $C_\lambda \text{ (Å)} = 1220\text{-}1800$.

Given these parameters space, we use the following steps to create the dataset for single Voigt profiles:

1. Generate the Voigt profiles using the ‘Faddeeva function’, for a randomly selected value of b and N_{HI} from the above range, resulting in optical depth (τ) over a velocity resolution of 0.6 km s^{-1} .
2. Convolve the simulated flux ($F = e^{-\tau}$) with the tabulated line spread function (LSF) of the HST COS spectrograph.⁴ The Line Spread Function (LSF) varies with each grating and is wavelength-dependent. Thus, the convolution depends on both the observed wavelength (z_{abs}) and the grating used.
3. We randomly select a central wavelength value (C_λ). For $C_\lambda > 1450\text{Å}$, a value of z_{abs} or z is selected randomly from a uniform sample between 0.2 to 0.47, and the grating is G160M. However, for central wavelength $\leq 1450\text{Å}$, z_{abs} are randomly selected from a uniform sample between 0.005 to 0.2, and grating is G130M. The convolution is performed in the observed frame.
4. Re-sample the convolved data to a similar wavelength scale ($\Delta\lambda = 0.0299 \text{ Å}$ i.e. $\Delta v = 6 \text{ km s}^{-1}$) with which D16 resampled their combined spectra.
5. Add Gaussian random noise to the simulated Voigt profile with a signal-to-noise ratio (SNR) selected from 5-100.
6. Convert the rest-wavelength to the Δv . We align the absorber at the center by selecting a chunk of 301 pixels and pad the rest of the chunk with continuum flux = 1.

After creating a sample of single absorption lines, we proceed with the following procedure to generate a sample representing double lines, which simulates blends of two components within an absorption system. Initially, we randomly select two simulated Voigt profiles with optical depths τ_1 and τ_2 from the first step. Each absorption line is then shifted by $\pm\Delta v/2$, where Δv is randomly chosen from the range of 5 to 350 km s^{-1} . This ensures that the center of the absorption line does not align closely with the spectral edges. Subsequently, the combined optical depth ($\tau = \tau_1 + \tau_2$) is converted into flux ($F = e^{-\tau}$), serving as the input for the second step. The procedures outlined above are similarly applied throughout.

Fig. 2 illustrates two examples of our simulated absorption lines. The left panel of Fig. 2 shows a single Voigt profile for a given b , N_{HI} and z_{abs} ; the right panel shows an overlapping double Voigt profile structure with velocity separation (Δv) for a given pair of b and N_{HI} . A solid brown line in Fig. 2 shows the simulated line generated in step (i). After convolving the line with COS LSF corresponding to step (ii) is shown in the green line. The red dashed line shows the final absorption lines after rebinning and adding the Gaussian noise.

The above-generated dataset is divided into 80% training and 20% testing datasets, covering the same parameter ranges. The ML models use the training dataset as input and evaluate their accuracy on new, unseen data with the testing dataset.

3.3. Mock data

Ideally, the accuracy of the ML algorithm should be consistent with simulated and real testing datasets. In the case of any disagreement, generating a mock dataset can effectively resolve any issues with the algorithm’s performance or the creation of the simulated testing dataset. Therefore, complementing our study of the *real* data, we also generate a set of *mock* testing data.

³ <https://archive.stsci.edu/prepds/igm/>

⁴ <https://spacetelescope.github.io/COS-Notebooks/LSF.html>

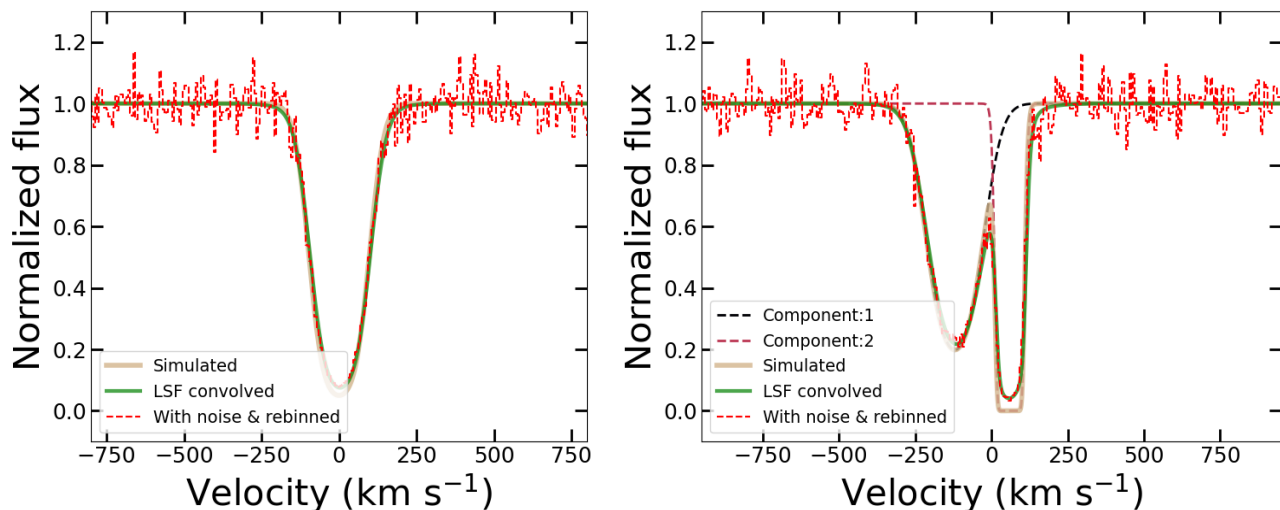


Fig. 2. *Left panel:* The brown line shows the simulated Voigt profiles for $N_{\text{HI}} = 10^{14} \text{ cm}^{-2}$, $b = 80 \text{ km s}^{-1}$. The green lines show the absorption lines after convolving with the HST’s tabulated LSF. The red dashed line shows the absorption line after adding the Gaussian noise (SNR=25) and rebinning it to a similar velocity frame as the HST data. This red dashed line represents the typical single absorption line used as the training dataset in this study. *Right panel:* Same as the left panel but a simulated double absorption line. The dashed lines show two simulated single absorption lines ($N_{\text{HI}} = 10^{14.29}$ and $10^{15.06} \text{ cm}^{-2}$, $b = 92.67$ and 25.43 km s^{-1}) that are shifted by $\pm\Delta v/2 \sim 75 \text{ km s}^{-1}$ value and the combined profile is shown in brown color. The training dataset for double absorption lines is shown in red dashed lines.

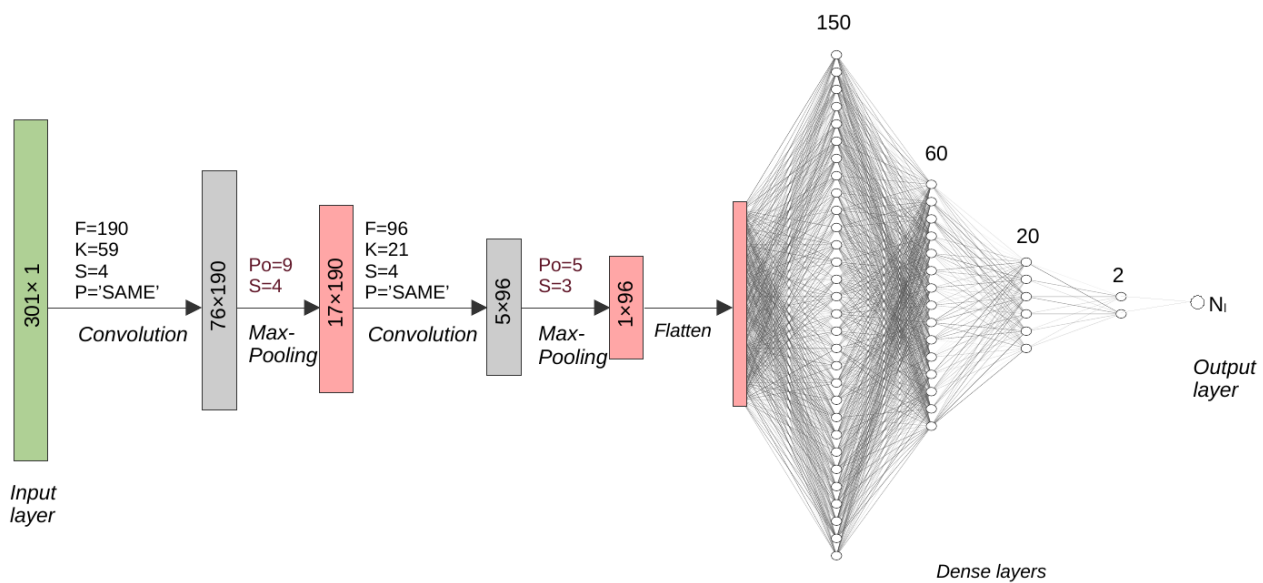


Fig. 3. Schematic diagram of the CNN architecture to classify the number of absorption lines. The terminology used here is F: Filter size, K: kernel size, S: strides, P: Padding, and Po: Pooling size. The number of neurons in the dense layers is written at the top. The last layer has one output varying between 0 and 1. The values < 0.5 are assigned $N_l = 1$, and values ≥ 0.5 are assigned $N_l = 2$.

These mock Ly α lines mimic the real dataset generated by the procedure discussed in Sect. 3.2. The mock absorption lines have exactly the same physical parameters (b , $\log N$, SNR, z and C_l) as the real dataset. In subsequent sections, we also assess the ML algorithm’s performance on this realistic mock data and demonstrate its reliability.

4. Classifying number of absorption lines

4.1. CNN architecture

This section introduces an ML algorithm based on CNN architecture, specifically designed for binary classification to identify the number of absorption lines. The input data consists of a training dataset generated in Sect. 3, comprising 301 pixels representing simulated absorption lines. The data labels are 0 for $N_l=1$ and 1 for $N_l=2$. The model’s output is a single value ranging between 0 and 1, where values $<$ a threshold value indicate a

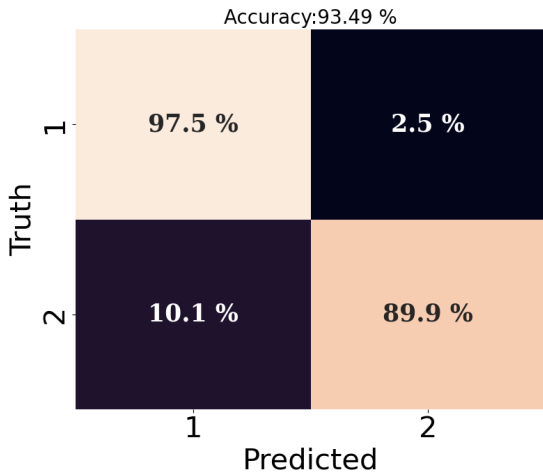


Fig. 4. Confusion matrix for the predictions for the number of absorption lines using the CNN (as shown in Fig. 3). The CNN was trained on 1.6 million lines and tested on 400K samples, with an equal number of single and double lines. We find the Sensitivity=97.47%, Specificity=89.92%, Precision=89.64% and Negative Predictive Value=97.55%.

single absorption line ($N_l=1$) and \geq threshold value corresponds to a double absorption line ($N_l=2$). We tested model outputs with various threshold values and found that 0.5 gives an unbiased result.

The CNN architecture shown in Fig. 3 includes an input layer with 301 neurons, two convolutional layers, two max-pooling layers, and four fully connected dense layers with a decreasing number of neurons. The activation function employed throughout the model is the *Leaky ReLU* (Eq. 1), except the *sigmoid* function (Eq. 2) in the last layer. We use the *binary cross-entropy* loss function and the *Adam* optimizer with a learning rate of 10^{-3} for optimization.

The CNN is trained on 1.6 million samples and tested on 4×10^5 samples (see Sect. 3), with an equal number of single and double absorption lines. We apply batch propagation with batch size 100 and implement early stopping criteria with a patience of 20 epochs. To ensure robustness and accurate identification of the number of Voigt profiles in a chunk of 301 pixels, we carefully fine-tune the parameters of the binary classification algorithm (Fig. 3). Our objective is to achieve an accuracy of over 90% (see Eq. 4) and F1-score greater than 0.8 (see Eq. 5).

We also tested with other ML algorithms, like random forest classifiers (Breiman 2001) and support vector machines (Cortes & Vapnik 1995). However, we found that the F1-score for all other classifiers was less than 0.8.

4.2. Classification of number of Ly α absorption lines

Fig. 4 shows the performance of the binary classification algorithm computed for the simulated test dataset. The simulated test sample has an impressive true positive (TP) rate of 97.5%, accurately identifying $N_l=1$ absorption lines. The false positive (FP) rate was 10.1%, reflecting a moderate number of misclassifications of $N_l=2$ absorption lines as $N_l=1$. However, the true negative (TN) rate was high at 89.9%, indicating a highly reliable identification of $N_l=2$ absorption lines. We also noted a small false negative (FN) rate of 2.5%, indicating a low number of misclassifications of $N_l=1$ absorption lines as $N_l=2$. The normalized confusion matrix (Fig. 4) demonstrates the binary classification

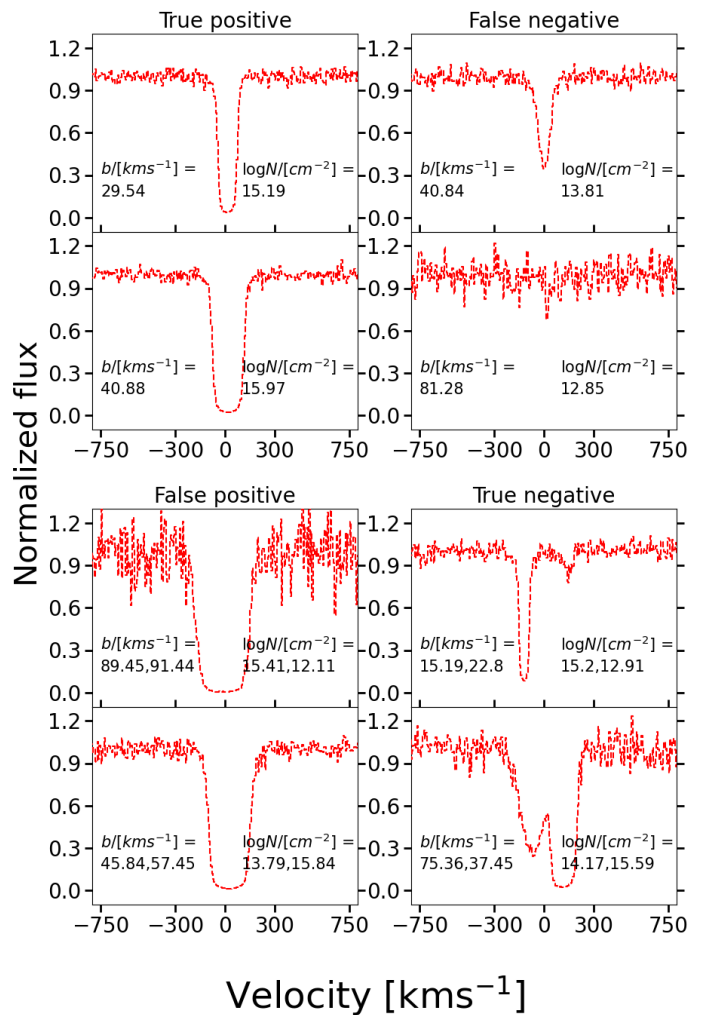


Fig. 5. Each panel shows two examples from the four classes of Fig. 4. The top left and bottom right panels show the correctly predicted single and double absorption lines. The top right and bottom left show the misclassified examples.

algorithm's ability to distinguish between the two absorption line categories. The caption mentions the values of sensitivity, specificity, precision, and negative predictive values. This leads to an F1-score (see Eq. 5) of 0.93, suggesting the model accurately identifies single and double absorption lines.

Fig. 5 shows two representative examples from each category. Even by visual inspection, it becomes evident that the misclassified absorption lines also appear visually ambiguous. We evaluated the model's performance across different parameters, including SNR, b -parameter, and N_{HI} as shown in Fig. 6. As expected, accuracies are notably lower for small values of SNR. This effect is also evident from the examples FP and FN in Fig. 5. However, excluding cases with $\text{SNR} < 20$ in the lower percentile consistently yields accuracies above 98% and 91% for single and double lines, which is promising. We also find that the accuracy for single lines is consistently better than accuracy for double lines. We also find that the accuracy decreases slightly with increasing Doppler width. This pattern is similar for column density for single lines but not for double lines.

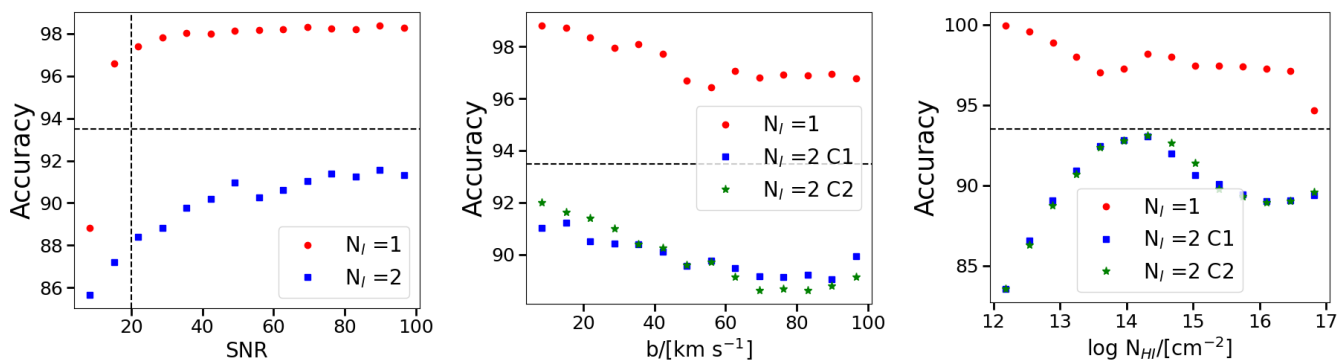


Fig. 6. Comparison of Accuracy Versus Signal-to-Noise Ratio (SNR), Doppler width (b) and column density (N_{HI}) for simulated data.

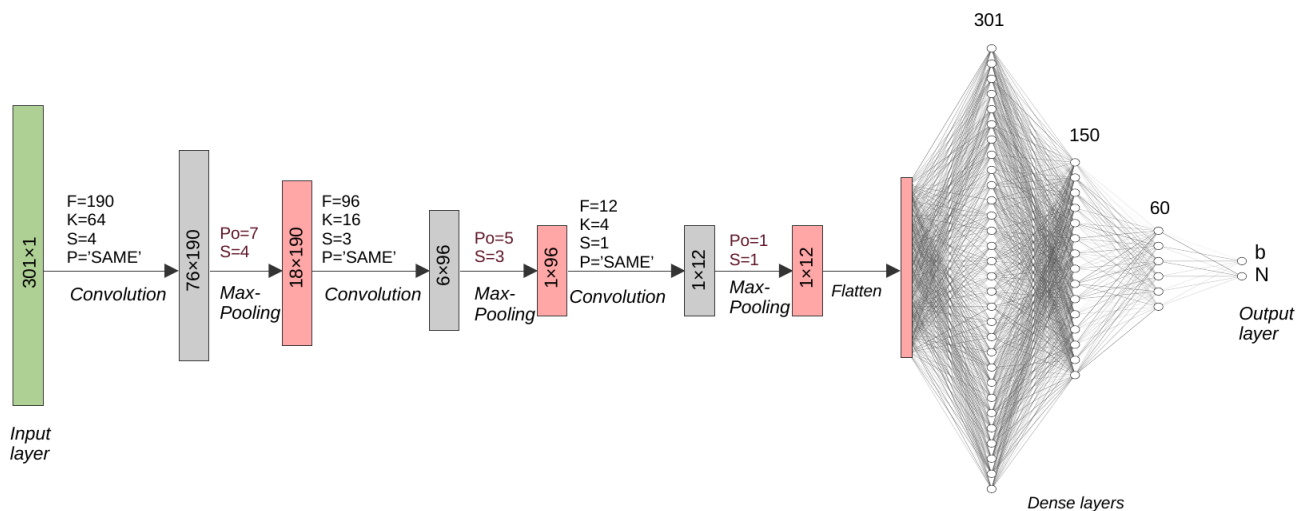


Fig. 7. Schematic diagram of the CNN model to predict the b and N values for a single absorption line. The CNN comprises three 1-dimensional convolutional layers, each followed by three max-pooling layers; after flattening, the input is input to 3 dense layers with a decreasing number of neurons and two neurons in the output layer.

The evaluation of the simulated test sample and the visual examination of classification examples highlight the CNN-based algorithm's effectiveness and reliability in absorption line classification tasks.

5. Regression analysis

5.1. Algorithm

In this section, we outline the regression analysis ML algorithm designed to determine the physical properties of absorption lines. We train this network on the simulated dataset generated in Sect. 3, similar to the previous model. The primary output predictions are the parameters characterizing the absorption lines. For single lines, these parameters encompass $\log N_{\text{HI}}$ (or $\log N$) and b , while for double lines, they extend to $\log N_1$, b_1 , $\log N_2$, b_2 (the sub-scripts represent components), and Δv .

To build the regression analysis, we initially experimented with fully connected deep neural networks with varying numbers of hidden layers and other units to develop the ML algorithm. However, we found that a large input dataset was required for the algorithm to learn effectively, which was computationally expensive. Therefore, to optimize the model's

learning efficiency, we use CNNs for parameter estimation. The architecture, illustrated in Fig. 7, comprises of:

- a *convolutional layer* with a *kernel size* of 64 pixels and *stride* of 4 pixels. This layer has 190 *filters*, which it applies to the absorption line, producing 190-channel data from the original 1D data,
- a *max pool layer* with a *pool size* of 7, the layer outputs the maximum value using a *stride* of 4 pixels,
- two layers [a] and [b] are repeated with decreasing number of *filters* and *pool size*,
- flattening* the output array so that the layer returns a single output served as an input to the fully connected dense layer,
- three fully connected *dense layers* with a decreasing number of neurons,
- the output layer, resulting in two output values.

The single absorption lines dataset consists of 2.5 million samples randomly divided into 80% as training and 20% as testing datasets. The data size was selected to minimize computational time and achieve higher accuracy. All the convolutional and dense layers are activated using the *LeakyReLU* activation function. We used the *Adam* optimizer with a 10^{-4} learning rate. The model undergoes training in batches of 10 instances, em-

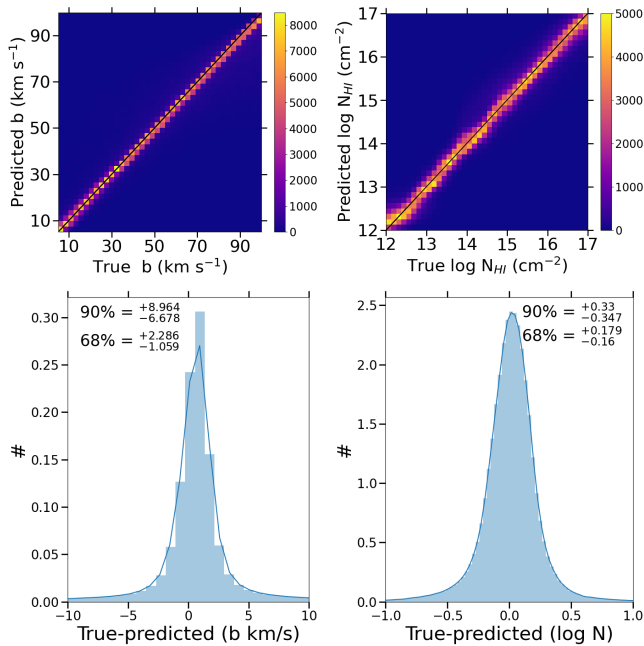


Fig. 8. The upper panel compares the actual and predicted values for the two parameters, b and N . The lower panel exhibits the distribution of the differences between the predicted and true values, with markers for the 90% and 68% percentiles.

employing early stopping with patience of 100 epochs. Training halts after 128 epochs based on the specified early stopping criteria. The weights are updated based on the MSE loss function. The hyper-parameters were varied to test the accuracy in order to keep hyper-parameters resulting in the highest accuracy.

For double absorption lines, the architecture was similar to the above CNN (Fig. 7) with minor modifications:

- To obtain similar outcomes, the input data consisted of a sample size of 4 million, split into two sets: 80% for training and 20% for testing.
- The output layer has five values (b_1 , b_2 , $\log N_1$, $\log N_2$ and Δv).
- Using early stopping criteria, we train the algorithm for 430 epochs.

5.2. Parameter estimation of the Ly α absorption lines

Fig. 8 shows the performance of the CNN model predicting the physical properties of the simulated test dataset of a single Ly α absorption line. The upper panels of Fig. 8 show the comparison between the true (horizontal axis) and predicted (vertical axis) values of Doppler width and column density for the test-simulated data. We find a tight correlation between the intrinsic and predicted parameters, indicating that our CNN model accurately predicts the physical properties of a single absorption line. The black line is the one-to-one line marking a perfect prediction. The figure shows a nominal scatter in the algorithm’s prediction of b and $\log N_{\text{HI}}$. We found negligible bias for the selected range of the parameters of b and $\log N_{\text{HI}}$.

The lower panels of Fig. 8 show the histogram of the difference between the true and predicted values of b and $\log N_{\text{HI}}$. We find that 90% of the predictions for the Doppler width (σ_{90b}) are within $+8.964$ km s^{-1} , and for column density (in log-scale, σ_{90N}) is within $+0.330$ cm^{-2} . The combined (σ_{90b} and σ_{90N}) outlier fraction with $|b_{\text{true}} - b_{\text{pred}}| > 7.8$ km s^{-1} along with $|N_{\text{true}} - N_{\text{pred}}| >$

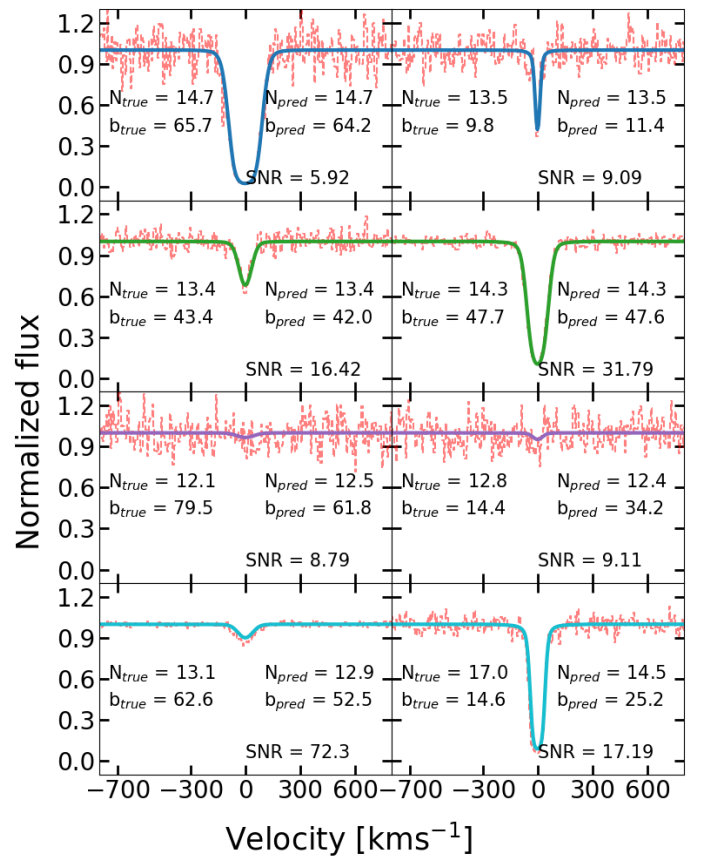


Fig. 9. The figure shows examples of the simulated test single absorption lines and the corresponding Voigt profile predicted by the CNN model (in colors). The input data, consisting of 301 pixels generated in Sect. 3, is shown in light red. The figures in the upper panel demonstrate precise physical parameter predictions made by the CNN for low SNR data (blue), while the second panel displays higher SNR data (green). The two lower panels illustrate two instances of an inaccurate prediction made by CNN for low (purple) and high SNR (cyan). To be considered an accurate prediction, the criterion is $|N_{\text{true}} - N_{\text{pred}}| < 0.33$ cm^{-2} and $|b_{\text{true}} - b_{\text{pred}}| < 7$ km s^{-1} . Whereas $|N_{\text{true}} - N_{\text{pred}}| \geq 0.33$ cm^{-2} and $|b_{\text{true}} - b_{\text{pred}}| \geq 7$ km s^{-1} serve as the criterion for non-accurate prediction.

$10^{0.33}$ cm^{-2} is less than 0.01%. This fraction reduces even further to only 0.0002% if we consider output only for samples with $\text{SNR} > 15$.

Fig. 9 demonstrates a few examples of the predictions by CNN for the single absorption test-simulated data. The input data, consisting of 301 pixels generated in Sect. 3, is shown in red dashed lines. The figures in the upper boxes demonstrate precise physical parameter predictions made by the CNN for low SNR data ($\text{SNR} < 10$; blue), while the second panel displays higher SNR data ($\text{SNR} > 10$; green). The two lower panels illustrate two instances of an inaccurate prediction made by CNN for low (purple) and high SNR (cyan).

The CNN results in similar accuracy for the test-simulated double absorption sample predictions as for the single absorption lines. The results comparing true and predicted values of b (b_1 and b_2), $\log N_{\text{HI}}$ (N_1 and N_2) and Δv are shown in the upper panel of Fig. 10. As seen from the upper panel of Fig. 10, the density of predicted values overlaps the true versus true one-to-one black line. The scatter of predicted values of $\log N$ for double lines has increased compared to the scatter for single absorption lines. However, we do not see any biases in the parameter’s predictions, even in double absorption lines. This alignment

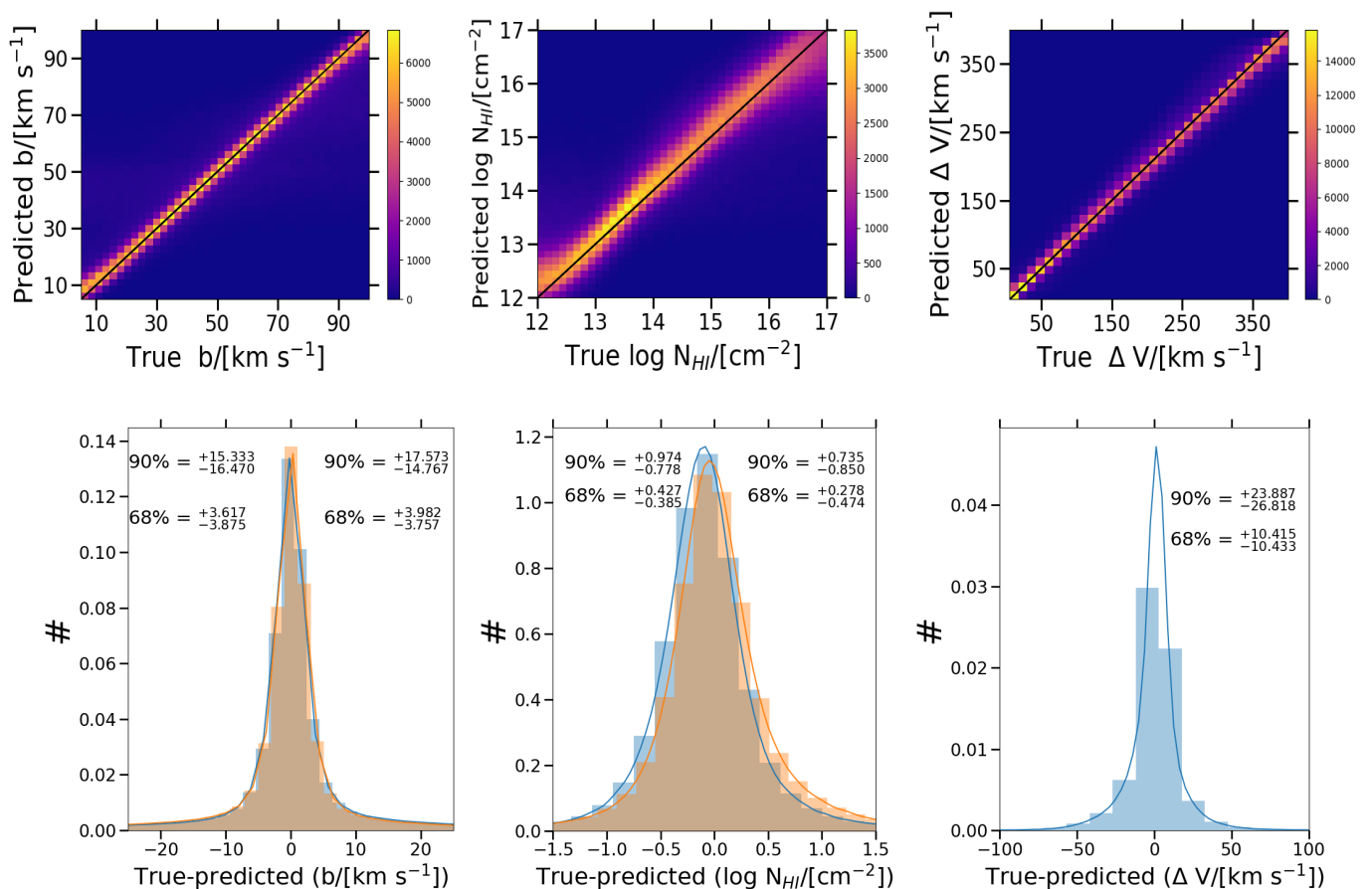


Fig. 10. Same as Fig. 8 but for a double absorption line. The upper left panel shows the true versus predicted values stacking b_1 and b_2 . Similarly, the upper middle panels show column density. The right upper panel shows the velocity difference between the two absorption lines. The lower panels show the histogram of the difference between true and predicted values, with 90% and 68% values marked at the top.

demonstrates the algorithm’s robustness in handling these more complex absorption profiles.

To test the algorithm’s performance, we show the difference between the true and predicted values in the lower panel of Fig. 10. The histogram shows that σ_{90b} for b_1 is within $+15.333$ to -16.470 km s⁻¹, for b_2 is within $+17.573$ to -14.767 km s⁻¹. Similarly σ_{90N} for $\log N_1/\text{cm}^{-2}$ within $+0.974$ to -0.778 for $\log N_2/\text{cm}^{-2}$ within $+0.735$ to -0.850 and for Δv is $+23.887$ to -26.818 km s⁻¹. The combined (σ_{90b} and σ_{90N}) outlier fraction with $|b_{\text{true}} - b_{\text{pred}}| > 16$ km s⁻¹ along with $|N_{\text{true}} - N_{\text{pred}}| > 10^{0.9}$ cm⁻² is less than 2.5%. This fraction reduces even further to only 1.5% if we consider output only for samples with SNR > 15.

A few examples of the double absorption test-simulated data with their predicted Voigt profiles are shown in Fig. 11. Noticeably, our ML model can accurately predict two parameters even if the double absorption lines are separated by small Δv . However, challenges arise when either the absorption lines are nearly saturated, or they are heavily obscured by noise, or there is a significant contrast in optical depth between two absorption lines with one almost buried in noise. These scenarios emphasize the CNN model’s limitations under specific circumstances and scope for improvement.

Based on this analysis, we conclude that our CNN models accurately predict the column density and Doppler width for single and double absorption lines. The minimal outliers confirm that CNN can robustly extract b and N_{HI} of the single and double absorption lines.

6. Application to the real data

The preceding sections show that our ML algorithm excels in its performance on simulated absorption lines designed to emulate the characteristics of real data obtained from the HST-COS, as detailed in Sect. 3. To evaluate the real-world applicability of our ML algorithm (Sect. 4 and Sect. 5), we now test it on Ly α line profiles obtained from the COS data (D16). To ensure compatibility, we chose observed data falling within a parameter range akin to the simulated data (as outlined in Section 3), in addition to 3σ detection according to the line detection criteria used in D16, resulting in 1364 absorption systems.

The line list files provided by D16⁵ include 2400 Ly α absorption lines. We examine the corresponding spectrum for each line to determine whether the Ly α line consists of single or multiple components. Our approach involves searching each line to identify if adjacent lines share common wavelengths. If the span of common wavelengths for absorption lines continuously touches the spectrum’s continuum (within error of the spectrum) for more than seven pixels (with each pixel being 0.035 Å), we classify these as single-component absorption lines. For the remaining lines, we count the number of lines meeting the aforementioned criteria. With this method, we find that out of 2400 components, approximately 1557 are Ly α lines with a single component, and 286 systems are identified as having double components. Following specific criteria ($5 \leq b/\text{km s}^{-1} \leq 100$, $12 \leq \log N/\text{cm}^{-2} \leq 17$, $5 \leq \text{SNR} \leq 100$ and discarding lines

⁵ available at <https://archive.stsci.edu/prepds/igm/>

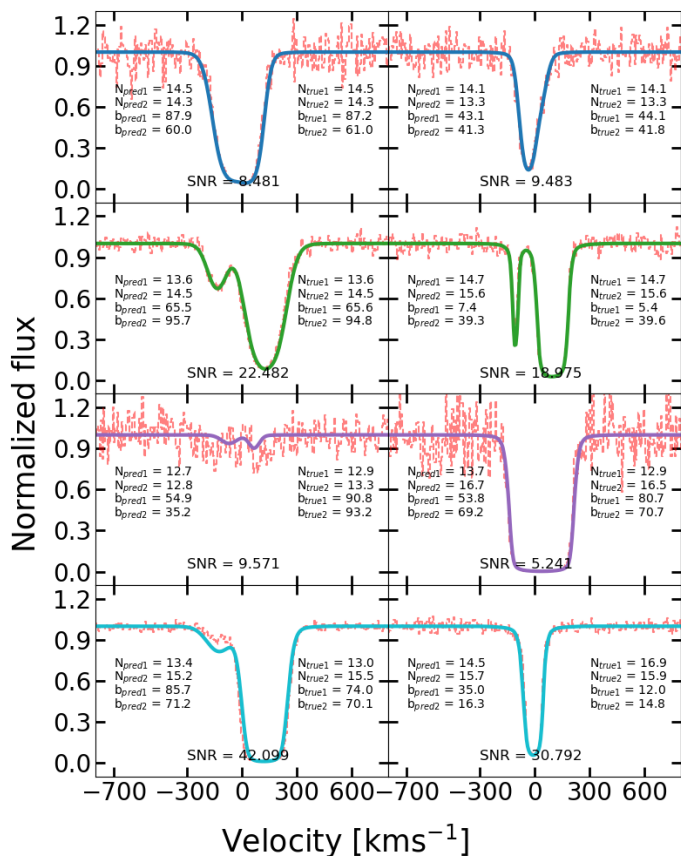


Fig. 11. Same as Fig. 9 but examples of the simulated test double absorption lines and the corresponding Voigt profile predicted by the CNN model (in solid colored lines).

with significance below 3σ), we selected 1364 lines for further analysis.

To use these absorption lines as inputs for our ML algorithms, we select a segment of the spectrum encompassing the absorption line and an adjacent line-free region. This segment is centered within a 301-pixel chunk. If the spectral segment does not span the entire 301 pixels, we pad the remaining locations with a continuum added with Gaussian random noise. The standard deviation of the noise in this padded area is determined based on the median of the error vector within the line-free region surrounding the absorption line. To assess the performance

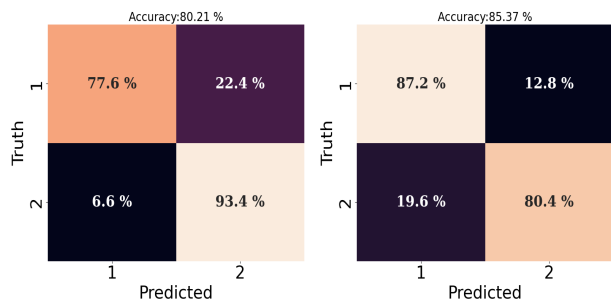


Fig. 12. The plot shows the prediction from the classification algorithm for the HST data with true labels from D16 (left) and G17 (right). For D16 [G17], we find the accuracy = 80.21% [85.37%], sensitivity=77.57% [87.24%], specificity=93.39% [80.41%], precision=98.33% [92.18%] and negative predictive value=45.40% [70.41%].

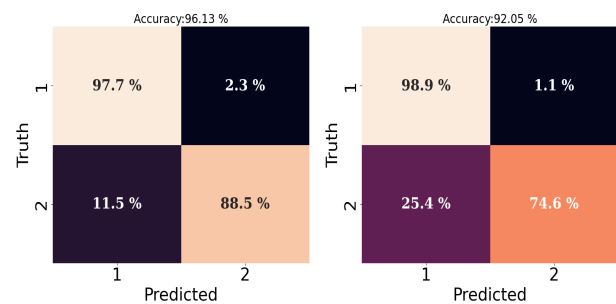


Fig. 13. Same as Fig. 12 but for the mock dataset. For D16 [G17], we find the accuracy = 96.13% [92.05%], sensitivity=97.71% [98.94%], specificity=88.50% [74.58%], precision=97.62% [90.79%] and negative predictive value=88.89% [96.54%].

of our ML algorithms on this dataset, we first apply our ML algorithm to these lines and record the results. For comparison purposes, we employ two distinct Voigt profile fitting algorithms. In addition to fitting done by D16, we also apply the VIPER algorithm (G17) to the same dataset.

Before analyzing the performance of our algorithms, it is important to highlight the differences in determining the number of components in absorption line systems between D16 and VIPER. Although VIPER adheres to the same significance level criteria for line identification as D16, their methods for determining whether lines are single or multi-component differ. D16 used additional spectral information, such as higher-order lines or coincidental metal lines, to determine if lines are single or multi-component. In contrast, VIPER employs the Akaike Information Criterion with Corrections (AICC) to decide the number of components. Furthermore, if AICC identifies more than one component, VIPER re-evaluates the significance level of all components, discarding any component with significance below 3σ . Due to these methodological variations, VIPER identifies 784 single lines and 296 double lines in the sample, differing from the 1137 single and 227 double lines found by D16.

Given that VIPER, like our ML algorithm, does not utilize additional spectral information for component identifications and relies solely on Ly α lines as input, we anticipate our algorithm to exhibit improved performance in classification when using VIPER labels as compared to D16 labels.

6.1. Performance on HST COS data: Classification

First, we use the classification algorithm (see Sect. 4.1) to test the accuracy in predicting the number of absorption lines for the COS data. Similar to Sect. 4.1, we input the normalized flux to the model, and the output is the number of absorption lines. We visualize the model’s performance by comparing the predicted labels with “true” labels obtained from the fits of D16 and VIPER.

In Fig. 12, we compare the results of our classification algorithm with the results of D16 (the left-hand panel) and VIPER (right-hand panel). In comparison, with D16, we find that the double lines are identified accurately (93.4%). However, there are 22% of single lines identified as double lines, resulting in the accuracy for single lines to be just 78%. Upon further investigation, we found that most of the 22% single lines (152 out of 255) that are identified as double lines have SNR < 20. The overall accuracy of our algorithm with respect to the classification of single versus double lines identified by D16 is 80.21%, whereas other metrics such as recall is 77.57%, F1-score is 0.86.

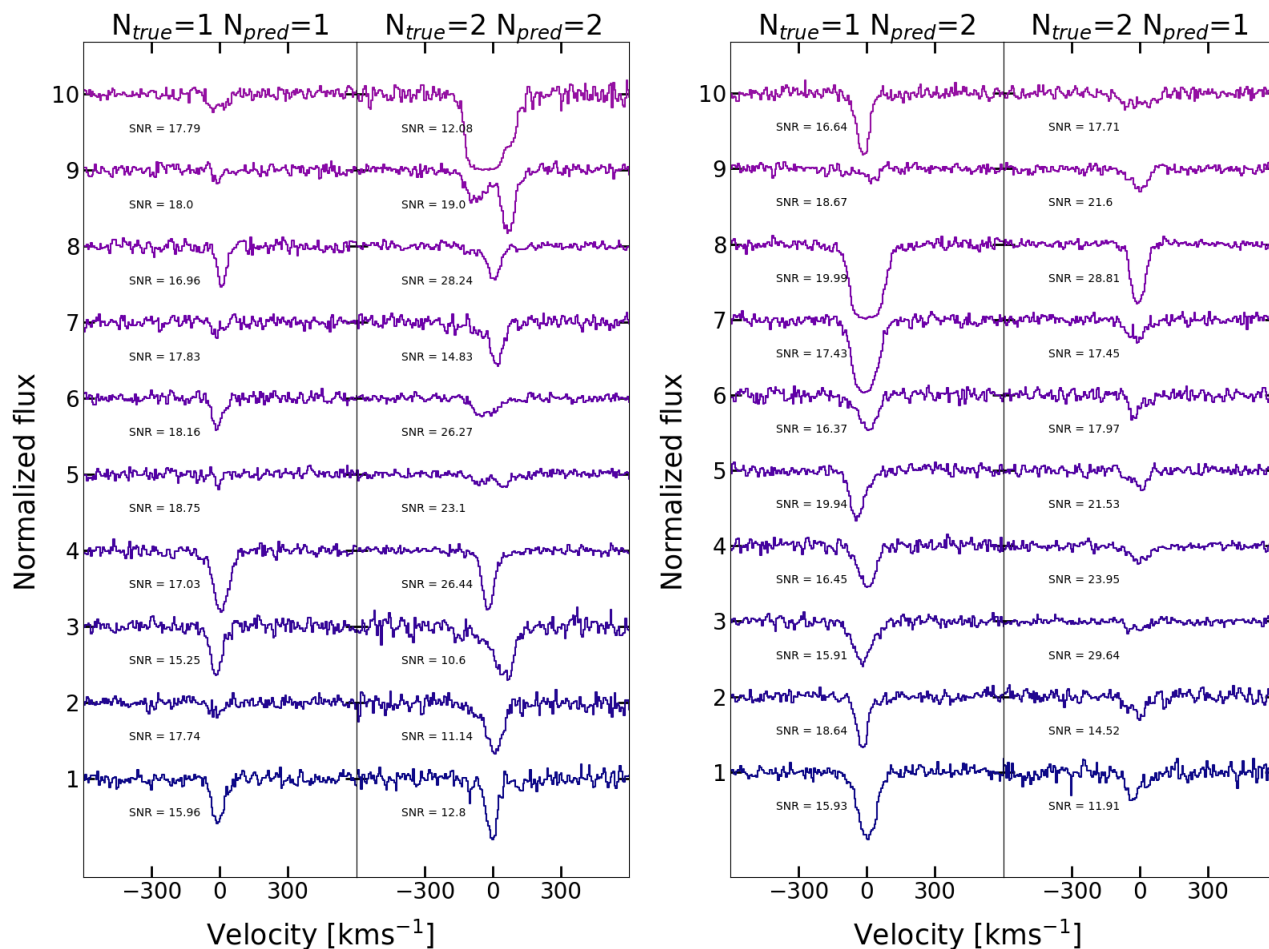


Fig. 14. *Left Panel:* Successful Classification - The panel displays instances where the classification algorithm accurately identifies single and double absorption lines, effectively matching the true labels. *Right Panel:* Misclassified Cases - The two panels show examples of the misclassified single and double absorption lines, highlighting areas for improvement in certain challenging scenarios.

In comparison with the results of VIPER (see the right-hand panel in Fig. 12), we find that 87% of the single lines are identified correctly, and only 13% were misclassified as double lines. For double lines, however, our algorithm could classify correctly for 80% of the lines and miss-classify 20% of the lines as single lines. 47 out of 58 misclassified double lines have $SNR < 20$. The overall accuracy of our algorithm with respect to the classification of single versus double lines identified by VIPER is 85.37%, which is better than the one obtained for identification D16, as per our expectations. Other metrics such as sensitivity (recall) is 87.24% and F1-score is 0.89.

Although our algorithm performs reasonably well, achieving an accuracy of 85% for labels from VIPER, this does not match the 93% accuracy obtained with our simulated data (refer to Fig. 4). The 8% decrease in accuracy is primarily due to a 10% reduction in true positives and true negatives for real data. We conducted a visual inspection of several instances where our algorithm was unsuccessful, yet we could not identify a clear reason for these failures. In many cases, the misclassifications appeared to stem from genuine confusion where double lines look single or are not prominent because of poor SNR. Examples of such cases, including those where the classification was accurate, are depicted in Fig. 14.

A potential reason for an 8-10% decrement in the performance of our algorithm on real data as compared to simulated data might be the inherent difficulty in emulating the real obser-

vations. To test this hypothesis, we decided to utilize our mock dataset (see Sect. 3.3) where we used exact same parameters of both D16 and VIPER fits, i.e., identifications as well as b and N_{HI} values and modeled instrument effects, noises, and central wavelength. We then input those in our classification algorithm and compared them with D16 and VIPER labels. In this case, our results are shown in Fig. 13. We find that the accuracy [F1-score] for D16 fits is 96.13% [.97], and VIPER fits is 92.05% [.94]. These accuracies are comparable to the accuracy obtained in the simulated data. Therefore, it seems our hypothesis is correct, and there are some subtle differences between emulating the real data and the real data. It is even more apparent for regression analysis, as discussed in the following subsection.

6.2. Performance on HST COS data: Regression

After testing the classification of absorption lines, we now analyze the performance of regression analysis on the identified absorption lines. This analysis entails utilizing flux data from D16 specifically for lines categorized as single (784) and double (296) by VIPER, totaling 1080 lines. Given the greater consistency observed in our classification algorithm with VIPER, we opt to utilize these line predictions. Among the 784 single lines, our classification model identified 684 as single lines and misclassified 58 double lines as single, resulting in a total of 742 single lines. Similarly, our model identified 238 double lines and

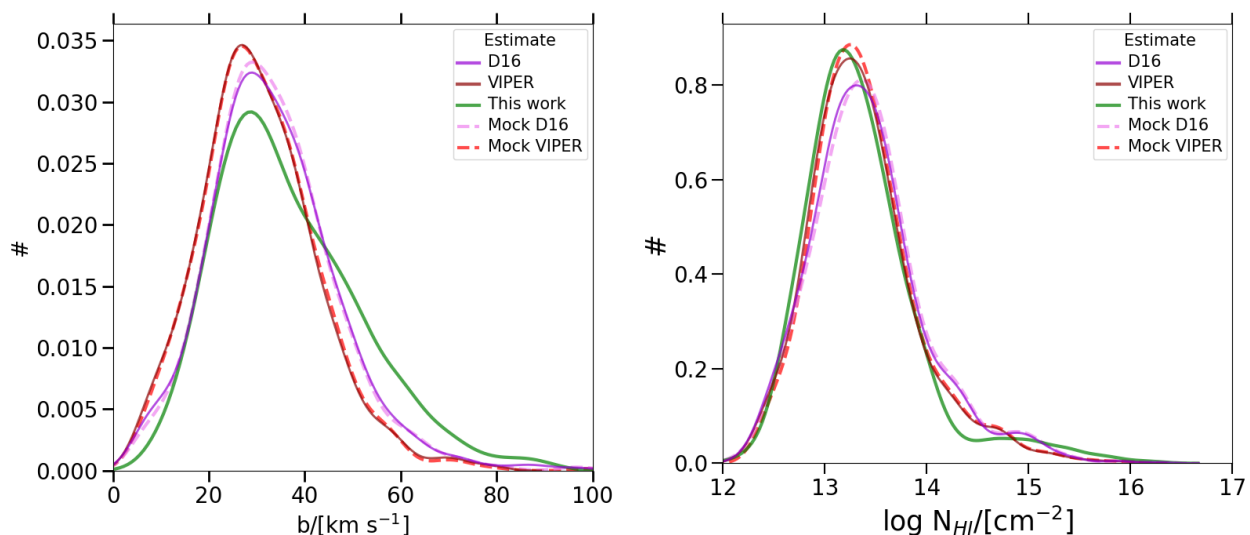


Fig. 15. The histograms show the distribution of b and $\log N_{\text{HI}}$ for a single absorption line estimated by the CNN model in this work (green) overlotted with distributions from (D16) (purple) and G17 (red). The distributions for the corresponding mocks are shown in dotted lines.

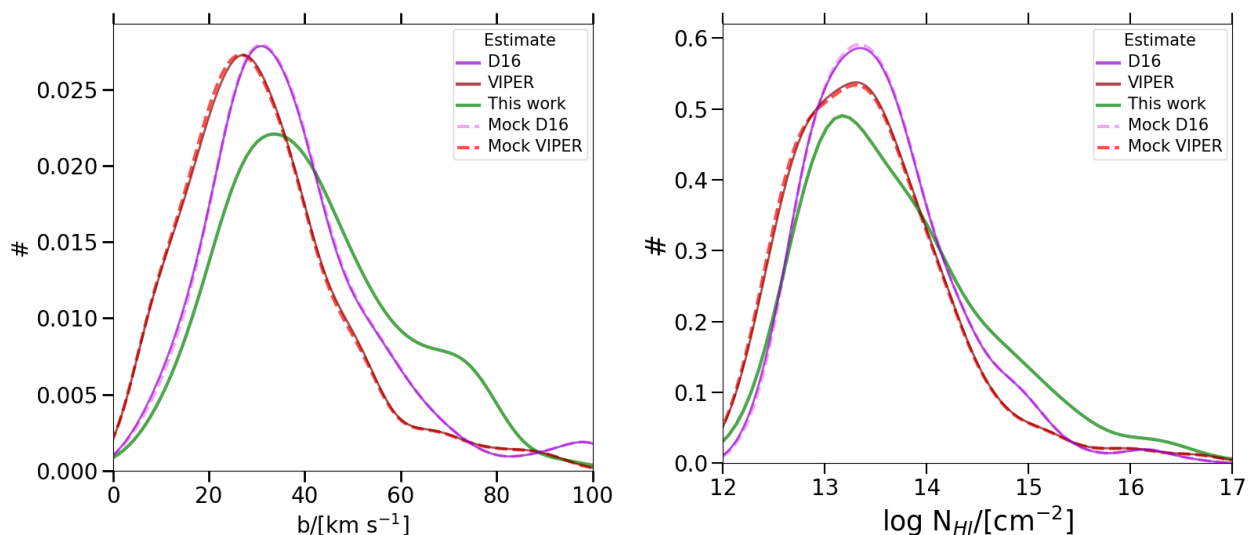


Fig. 16. Same as Fig. 15 but for parameters extracted from double absorption lines.

miscategorized 100 single lines as double lines, resulting in a total of 338 double lines.

First, we feed the single lines to our algorithm that predicts the values of b and N_{HI} . We show the distribution of predicted b and N_{HI} Fig. 15. We compare these distributions (green lines) with the values derived from VIPER (red lines) and D16 (purple lines). The distribution of b values estimated by the three studies is depicted in the left panel of Fig. 15. While the predicted b distribution shares qualitative similarities with both D16 and VIPER, there are noticeable differences. Firstly, the peaks of the distributions differ due to variations in the number of single lines across these studies. Specifically, D16 reports 1137 single lines, VIPER identifies 784 single lines, and our classification model detects 742 single lines. Secondly, our predicted b values align well with those of D16 for $b < 25 \text{ km s}^{-1}$, but we observe higher b estimates for wider Doppler widths. Notably, nearly 70% of the single lines exhibit $b > 25 \text{ km s}^{-1}$, among which 76% have $\text{SNR} < 20$. The right panel of Fig. 15 illustrates the distributions of N_{HI} . Our predictions demonstrate remark-

able consistency with the N_{HI} distribution from VIPER, whereas slight differences are observed compared to D16.

We extend the evaluation of the ML algorithm to lines identified as double absorption lines. These lines entail physical parameters including b_1 , b_2 , N_1 , N_2 , and Δv . In the left panel of Fig. 16, we present the stacked values of b_1 and b_2 , while the right panel illustrates stacked values of $\log N_1$ and $\log N_2$. Our estimates by the ML algorithm reveal that the predicted b values are notably higher than the estimations provided by both D16 and VIPER. Similarly, the N_{HI} estimates generated by our ML algorithm consistently exceed those obtained by VIPER. A contributing factor to this overestimation appears to be the misclassification of single lines as double lines by the classification algorithm. Out of a total of 338 lines predicted as double lines by our ML algorithm, 100 are misclassified single lines. However, even upon removing these misclassified lines, the differences in estimates do not diminish significantly. Moreover, from our simulated test data, our results of predicted parameters for double lines (Fig. 10) are slightly worse than those for single

lines (Fig. 8), suggesting that the predictions for double lines are expected to be less accurate than those for single lines.

Overall, our analysis reveals that while our algorithm performs reasonably well for single lines, it falls short of the performance achieved by D16 and VIPER in accurately reproducing the b and N values for double lines. This discrepancy highlights that part of the issue lies within our classification algorithm, which does not perform as anticipated. To further investigate, we tested our regression algorithms on the mock datasets we had prepared. In these tests, as highlighted in the previous section, the classification algorithm shows performance in line with expectations.

In Fig. 15 and Fig. 16, we show the predictions for the mock datasets as well. The dashed lines show the parameter estimates for the mock dataset, with purple color showing mock generating using D16 and red showing VIPER. The parameters predicted for the mocks almost overlap with the corresponding parameters for the real observed data. This consistency again underscores the challenge of simulating real observations accurately. Minor inconsistencies between the mock and real data primarily arise in cases of very low signal-to-noise ratio (SNR < 10). However, these mock tests unequivocally demonstrate the successful prediction of b and N_{HI} parameters by our ML algorithm, particularly when the simulated training dataset closely resembles the test dataset.

The successful application of regression analysis to both real observed data and mock data, in conjunction with the prior classification of absorption lines, validates the effectiveness of our comprehensive approach. Our study demonstrates that the ML algorithm yields statistically comparable results to traditional fitting methods. Furthermore, its minimal computational time renders it highly advantageous for large datasets. For instance, while manually fitting a Voigt profile takes at least 1-2 minutes and semi-automated codes like VIPER require 1-2 seconds, the ML algorithm can provide this information in just 0.0002 seconds. This efficiency underscores the potential of ML in efficiently managing complex absorption line analysis, especially considering the substantial demands of data processing.

7. Main Results and Discussion

The low-redshift ($z < 1$) Ly α forest is crucial for understanding the evolution of the IGM, galaxy formation, and unresolved baryon fractions. Despite its significant potential, extracting information from the Ly α forest presents considerable challenges, especially when using Voigt profile fitting for its numerous absorption lines. Therefore, developing an ML algorithm for Voigt profile fitting is essential for the success of upcoming large astronomical surveys.

In this study, we have developed a two-part ML algorithm, FLAME, using CNNs to identify the number of Voigt profiles that best fit a given Ly α absorption system and then determine the b and N_{HI} for each profile (see Fig. 1). We trained these CNNs with approximately 10^6 low- z Voigt profiles, synthesized to mimic real data from HST-COS. Given that the majority (96%) of the Ly α lines in the existing high SNR HST-COS data can be fitted with single or double-line profiles (see D16 and G17), we designed our first ML algorithm to classify the lines as either single or double profiles. The second stage of our ML algorithm comprises two networks: the first targets single-line profiles to determine b and N_{HI} , while the second is tailored for double-line profiles, determining b and N_{HI} for both components, as well as their velocity separation.

Evaluating the algorithms on simulated Ly α lines showcases its impressive performance. The classification algorithm (Fig. 3) correctly identifies $\geq 98\%$ of the single absorptions and $\geq 90\%$ of the double lines. Additionally, the accuracy increases with SNR (see Fig. 6). The regression algorithms in the second stage for single Voigt profiles determine values of b and N_{HI} robustly. For 90% of the single lines, the predicted b values lie within $+8.964$ km s $^{-1}$ and $\log N_{\text{HI}}$ (in log-scale) within $+0.330$ cm $^{-2}$ of the true values. Whereas for 90% of double lines the regression algorithm predicts, b within $\sim +16.453$ km s $^{-1}$, $\log N_{\text{HI}}$ within $+0.855$ cm $^{-2}$ and velocity separation of both lines Δv within $+23.887$ km s $^{-1}$ of the true values. The model demonstrates a close match between predicted and actual parameters, confirming its accuracy. The minimal scatter and negligible bias in predictions underscore its reliability across a broad range of parameters. Nonetheless, the model shows limitations with nearly saturated lines, data with high noise levels, or significant optical depth contrasts, suggesting areas for further enhancement.

We evaluated the performance of our ML algorithms across different parameters, including SNR, b -parameter, N_{HI} , and the velocity difference (Δv) between two absorption lines. Fig. 6 shows the accuracy trends with respect to these parameters. As expected, accuracies are notably lower for small values of SNR in simulated datasets. However, excluding cases with these parameters in the lower percentile (SNR > 20) consistently yields accurate accuracy above 94.2%, which is promising. Though in this analysis, we test for the wide range of parameters, however, if we established thresholds for these parameters, indicating conditions under which the model provides accurate estimates for b , N_{HI} , and SNR above 97.5%. The identified thresholds are as follows: SNR > 20 , b -parameter < 40 km s $^{-1}$ and $N_{\text{HI}} < 14$ cm $^{-2}$.

We applied the algorithm to HST-COS data, focusing on a selected subset of 1,400 absorption lines, and evaluated its performance against two methods of Voigt profile fitting: one using the fits provided by D16 and the other using the automated Voigt profile fitting code VIPER (G17). We observed that the accuracy of our classification algorithm decreased by approximately 10% compared to the simulated dataset. Specifically, we achieved an accuracy of 80% in comparison with the fits by D16 and 85% when compared with the fits from VIPER. Nevertheless, the regression algorithms showed reasonably good agreement in predicting b and N_{HI} values, closely matching their distributions from both VIPER and D16. Any discrepancies in the distribution mainly arise from the inherent difficulty in emulating the real observations.

In all our trials, we observed that the real dataset exhibits reduced accuracy compared to the simulated dataset. To understand the reasons behind the lower accuracy of our algorithms on real data, we generated mock data mirroring the parameters of real data fits from both D16 and VIPER. Applying our algorithm to this mock data, we found that the accuracy remains stable, showcasing a remarkable agreement between the predicted number of lines in the profiles and the values of b and N_{HI} . This finding suggests that the differences in accuracies between simulated and real datasets can be ascribed to the inherent complexities in modeling real data, which often contain nuances difficult to replicate accurately in simulations.

The simulated data may fall short of capturing the complexities, variations, and noise inherent in the real data. For example, accurately replicating the inherent noise patterns and instrument-specific calibration errors in simulations is extremely challenging. Strategies such as incorporating a fraction of real data into the training set may not yield the desired effectiveness in this

case, as the real data sample size is much lower compared to the size of the simulated data used in this analysis. The ongoing and upcoming large-scale spectroscopic surveys, such as DESI, 4MOST, WEAVE, and PFS, are designed to enhance the availability of real spectra significantly. This influx of real data is expected to play a crucial role in enabling machine learning models to improve their performance further.

Our study highlights the effectiveness of ML in analyzing Ly α absorption lines in quasar spectra, showcasing capability for both classifying the number of lines and estimating physical parameters. Through evaluations with real and mock data, we have shown that ML not only matches the accuracy of traditional methods but also significantly reduces computational effort, proving especially beneficial for large datasets where traditional approaches falter due to time and labor demands.

8. Summary

We present FLAME, a two-part ML algorithm to fit low- z Ly α absorption lines using CNNs. This algorithm effectively determines the optimal number of Voigt profiles for Ly α absorption systems and determines the Doppler parameter b and neutral hydrogen column density N_{HI} for each profile. It shows impressive accuracy, correctly identifying over 98% of single absorptions and over 90% of double lines in simulated data, which mimics the real Ly α absorption lines from HST-COS. For 90% of single lines, the FLAME accurately predicts b values within $\approx \pm 8$ km s $^{-1}$ and $\log N_{\text{HI}}/\text{cm}^2$ values within $\approx \pm 0.3$. For double lines, it shows slightly lower accuracy predicting b within $\approx \pm 15$ km s $^{-1}$ and $\log N_{\text{HI}}/\text{cm}^2$ within $\approx \pm 0.8$.

Despite its impressive performance on simulated data, FLAME's accuracy decreased for classifying lines by about 10% when applied to real HST-COS data. Nevertheless, there is reasonable agreement between the predicted b and N_{HI} distributions with other Voigt profile fitting algorithms such as VIPER (G17) and the fits from D16.

Our analysis with mock HST-COS data, crafted to reflect the parameters of real data, showed that FLAME can maintain stable accuracy, mirroring its success with simulated datasets. This underscores that the primary discrepancies in accuracy between simulated and real data stem from the challenges in fully capturing the complexities of real data in the simulated training dataset. Despite these hurdles, FLAME affirmatively demonstrates the feasibility of employing ML to fit Voigt profiles, highlighting the potential for ML in analyzing absorption lines.

Moving forward, we aim to refine FLAME, particularly to improve its performance with real data. Our efforts will include examining the specific challenges posed by real data and assessing how these affect accuracy. Including additional spectral information, such as metal lines, similar to the approach taken by D16, appears to be a promising method for enhancing accuracy. Additionally, incorporating real data into our training samples is a key strategy we believe will help align FLAME more closely with practical applications. The upcoming influx of data from spectroscopic surveys like DESI, 4MOST, WEAVE, and PFS is expected to benefit ML models significantly by providing richer training datasets. This effort will lead to more precise characterizations of the Ly α forest by FLAME.

Acknowledgements

PJ acknowledges Dr. hab Maciej Bilicki for useful discussion. The Polish National Science Center supported PJ through

grant no. 2020/38/E/ST9/00395. A partial finances during the manuscript are supported by the Young Scientist Award 2023, won by PJ. PJ acknowledges the CFT and ARIES computer facility to provide high-performance computers. MV acknowledges support from DST-SERB in the form of a core research grant (CRG/2020/1657). The authors acknowledge the assistance of tools such as Grammarly and ChatGpt in polishing the text at various places.

References

- Abadi, M., Agarwal, A., Barham, P., et al. 2015, TensorFlow: Large-Scale Machine Learning on Heterogeneous Systems, software available from tensorflow.org
- Akhazhanov, A., More, A., Amini, A., et al. 2021, arXiv e-prints, arXiv:2109.09781
- Alam, S., Aubert, M., Avila, S., et al. 2021, *Phys. Rev. D*, **103**, 083533
- Bainbridge, M. B., & Webb, J. K. 2017, *Monthly Notices of the Royal Astronomical Society*, **468**, 1639
- Baur, J., Palanque-Delabrouille, N., Yèche, C., et al. 2017, *jcip*, **2017**, 013
- Becker, G. D., Hewett, P. C., Worseck, G., & Prochaska, J. X. 2013, *Monthly Notices of the Royal Astronomical Society*, **430**, 2067
- Bolton, A. S., Schlegel, D. J., Aubourg, É., et al. 2012, *AJ*, **144**, 144
- Bolton, J. S., Gaikwad, P., Haehnelt, M. G., et al. 2022, *MNRAS*, **513**, 864
- Bolton, J. S., & Haehnelt, M. G. 2007, *MNRAS*, **382**, 325
- Bolton, J. S., Puchwein, E., Sijacki, D., et al. 2017, *MNRAS*, **464**, 897
- Bolton, J. S., Viel, M., Kim, T. S., Haehnelt, M. G., & Carswell, R. F. 2008, *MNRAS*, **386**, 1131
- Bosman, S. E. I., Fan, X., Jiang, L., et al. 2018, *MNRAS*, **479**, 1055
- Breiman, L. 2001, *Machine Learning*, **45**, 5
- Busca, N. G., Delubac, T., Rich, J., et al. 2013, *A&A*, **552**, A96
- Carswell, R. F., & Webb, J. K. 2014, VPFIT: Voigt profile fitting program
- Cheng, T.-Y., Cooke, R. J., & Rudie, G. 2022, *MNRAS*, **517**, 755
- Cortes, C., & Vapnik, V. 1995, *Machine learning*, **20**, 273
- Danforth, C. W., Keeney, B. A., Tilton, E. M., et al. 2016, *ApJ*, **817**, 111
- Davé, R., Anglés-Alcázar, D., Narayanan, D., et al. 2019, *MNRAS*, **486**, 2827
- de Dios Rojas Olvera, J., Gómez-Vargas, I., & Vázquez, J. A. 2021, arXiv e-prints, arXiv:2112.12645
- de Graaff, A., Cai, Y.-C., Heymans, C., & Peacock, J. A. 2019, *Astronomy & Astrophysics*, **624**, A48
- de Jong, R. S., Bellido-Tirado, O., Chiappini, C., et al. 2012, in *Society of Photo-Optical Instrumentation Engineers (SPIE) Conference Series*, Vol. 8446, *Ground-based and Airborne Instrumentation for Astronomy IV*, ed. I. S. McLean, S. K. Ramsay, & H. Takami, 84460T
- Eilers, A.-C., Davies, F. B., & Hennawi, J. F. 2018, *ApJ*, **864**, 53
- Fan, X., Strauss, M. A., Becker, R. H., et al. 2006, *AJ*, **132**, 117
- Flaugher, B., & Bebek, C. 2014, in *Ground-based and Airborne Instrumentation for Astronomy V*, ed. S. K. Ramsay, I. S. McLean, & H. Takami, Vol. 9147, International Society for Optics and Photonics (SPIE), 91470S
- Gaikwad, P., Choudhury, T. R., Srianand, R., & Khaire, V. 2017, arXiv:1705.05374v2, arXiv:1705.05374
- Gaikwad, P., Srianand, R., Choudhury, T. R., & Khaire, V. 2017, *Monthly Notices of the Royal Astronomical Society*, **467**, 3172
- Gaikwad, P., Srianand, R., Haehnelt, M. G., & Choudhury, T. R. 2021, *MNRAS*, **506**, 4389
- Gholamalinezhad, H., & Khosravi, H. 2020, Pooling Methods in Deep Neural Networks, a Review, arXiv:2009.07485 [cs.CV]
- Goodfellow, I., Bengio, Y., & Courville, A. 2016, *Deep Learning* (MIT Press)
- Gurvich, A., Burkhart, B., & Bird, S. 2017, *ApJ*, **835**, 175
- Hiss, H., Walther, M., Hennawi, J. F., et al. 2018, *apj*, **865**, 42
- Hopkins, P. F., Hernquist, L., Cox, T. J., & Kereš, D. 2008, *ApJS*, **175**, 356
- Hossin, M., & M.N, S. 2015, *International Journal of Data Mining & Knowledge Management Process*, **5**, 01
- Hu, T., Khaire, V., Hennawi, J. F., et al. 2023, arXiv preprint arXiv: 2311.17895
- Huang, L., Croft, R. A. C., & Arora, H. 2021, *Monthly Notices of the Royal Astronomical Society*, **506**, 5212
- Iršič, V., Viel, M., Haehnelt, M. G., et al. 2017, *prd*, **96**, 023522
- Khaire, V. 2017, *MNRAS*, **471**, 255
- Khaire, V., Hu, T., Hennawi, J. F., et al. 2023, arXiv e-prints, arXiv:2311.08470
- Khaire, V., & Srianand, R. 2015, *ApJ*, **805**, 33
- Khaire, V., Walther, M., Hennawi, J. F., et al. 2019, *MNRAS*, **486**, 769
- Kingma, D. P., & Ba, J. 2014, Adam: A Method for Stochastic Optimization
- Krogager, J.-K. 2018, VoigtFit: A Python package for Voigt profile fitting, arXiv:1803.01187 [astro-ph.IM]
- LeCun, Y., Bengio, Y., & Hinton, G. 2015, *Nature*, **521**, 436
- Lee, J., & Shin, M.-S. 2021, *AJ*, **162**, 297

- Liang, C., & Kravtsov, A. 2017, BayesVP: a Bayesian Voigt profile fitting package, [arXiv:1710.09852 \[astro-ph.GA\]](#)
- Lidz, A., Furlanetto, S. R., Oh, S. P., et al. 2011, *apj*, 741, 70
- Liu, T., Cao, S., Zhang, S., et al. 2021, *European Physical Journal C*, 81, 903
- Macquart, J. P., Prochaska, J. X., McQuinn, M., et al. 2020, *Nature*, 581, 391
- Madau, P., & Dickinson, M. 2014, *ARA&A*, 52, 415
- Matoba, K., Dimitriadis, N., & Fleuret, F. 2022, [ArXiv, abs/2203.01016](#)
- McDonald, P., Seljak, U., Burles, S., et al. 2006, *apjs*, 163, 80
- McQuinn, M., Lidz, A., Zaldarriaga, M., et al. 2009, *ApJ*, 694, 842
- Meiksin, A. A. 2009, *Reviews of Modern Physics*, 81, 1405
- Parhi, R., & Nowak, R. 2019, *IEEE Signal Processing Letters*, 27, 1779
- Parks, D., Prochaska, J. X., Dong, S., & Cai, Z. 2018, *Monthly Notices of the Royal Astronomical Society*, 476, 1151
- Pieri, M. M., Bonoli, S., Chaves-Montero, J., et al. 2016, in SF2A-2016: Proceedings of the Annual meeting of the French Society of Astronomy and Astrophysics, ed. C. Reyl e, J. Richard, L. Cambr esy, M. Deleuil, E. P econtal, L. Tresse, & I. Vauglin, 259
- Rauch, M. 1998, *ARA&A*, 36, 267
- Schaye, J. 2001, *ApJ*, 559, 507
- Shull, J. M., France, K., Danforth, C. W., Smith, B., & Tumlinson, J. 2010, *ApJ*, 722, 1312
- Shull, J. M., Harness, A., Trenti, M., & Smith, B. D. 2012, *ApJ*, 747, 100
- Springel, V. 2005, *MNRAS*, 364, 1105
- Stemock, B., Churchill, C. W., Lee, A., et al. 2023, [arXiv e-prints, arXiv:2311.16029](#)
- Tanimura, H., Aghanim, N., Douspis, M., Beelen, A., & Bonjean, V. 2019, *A&A*, 625, A67
- Tillman, M. T., Burkhart, B., Tonnesen, S., et al. 2022, [arXiv e-prints, arXiv:2210.02467](#)
- Vattis, K., Toomey, M. W., & Koushiappas, S. M. 2021, *Phys. Rev. D*, 104, 123541
- Veiga, M. H., Meng, X., Gnedin, O. Y., Gnedin, N. Y., & Huan, X. 2021, [arXiv e-prints, arXiv:2107.09082](#)
- Viel, M., Haehnelt, M. G., Bolton, J. S., et al. 2017, *MNRAS*, 467, L86
- Viel, M., Schaye, J., & Booth, C. M. 2013, *mnras*, 429, 1734
- Walther, M., O norbe, J., Hennawi, J. F., & Luki c, Z. 2019, *ApJ*, 872, 13
- Weinberger, R., Springel, V., Hernquist, L., et al. 2017, *MNRAS*, 465, 3291
- Worseck, G., Prochaska, J. X., McQuinn, M., et al. 2011, *ApJ*, 733, L24
- Y eche, C., Palanque-Delabrouille, N., Baur, J., & du Mas des Bourboux, H. 2017, *jcap*, 2017, 047
- You, Y., Gitman, I., & Ginsburg, B. 2017, [arXiv e-prints, arXiv:1708.03888](#)